In Vivo Transcranial Acoustoelectric Brain Imaging of Different Deep Brain Stimulation Currents

Yijie Zhou, Yibo Song, Shasha Qi, Xizi Song, *Member, IEEE*, Minpeng Xu, *Senior Member, IEEE*, Feng He, and Dong Ming, *Senior Member, IEEE*

Abstract—**Deep brain stimulation (DBS) is an effective treatment for neurologic disease and its clinical effect is highly dependent on the DBS leads localization and current stimulating state. However, standard human brain imaging modalities could not provide direct feedback on DBS currents spatial distribution and dynamic changes. Acoustoelectric brain imaging (AEBI) is an emerging neuroimaging method that can directly map current density distribution. Here, we investigate *in vivo* AEBI of different DBS currents to explore the potential of DBS visualization using AEBI. According to the typical DBS stimulus parameters, four types of DBS currents, including time pattern, waveform, frequency, and amplitude are designed to implement AEBI experiments in living rat brains. Based on acoustoelectric (AE) signals, the AEBI images of each type DBS current are explored and the resolution is quantitatively analyzed for performance evaluation. Furthermore, the AE signals are decoded to characterize DBS currents from multiple perspectives, including time-frequency domain, spatial distribution, and amplitude comparison. The results show that *in vivo* transcranial AEBI can accurately locate the DBS contact position with a millimeter spatial resolution (<2 mm) and millisecond temporal resolution (<10 ms). Besides, the decoded AE signal at DBS contact position is capable of describing the corresponding DBS current characteristics and identifying current pattern changes. This study first validates that AEBI can localize *in vivo* DBS contact and characterize different DBS currents. AEBI is expected to develop into a noninvasive DBS real-time monitoring technology with high spatiotemporal resolution.**

Index Terms—**Electroencephalography, acoustoelectric brain imaging, deep brain stimulation, current characteristics.**

I. Introduction

DEEP brain stimulation (DBS) is an effective treatment which has been applied to alleviate symptoms from neurological diseases [1]. Its clinical effect is highly dependent on the DBS leads localization and current stimulating state in the targeted brain region [2]. Postoperative migration, rotation and corrosion of DBS leads may decrease the overall therapeutic effect [3], [4], [5]. Corrosion of chronically implanted electrodes can cause impedance drift which affects optimal stimulation state of the preset current [3], [6]. Migration and rotation of DBS leads can both reduce the DBS therapeutic effect and induce other adverse effects by leading current to nontarget brain regions [4], [5]. Therefore, it is critical to visualize the currents directly and safely from DBS contacts to provide feedback for DBS real-time monitoring and optimization.

Previous works mainly reconstructed electrode localization and estimated volume of tissue activated around the electrodes from magnetic resonance imaging (MRI) and computed tomography (CT) scans [7], [8], [9], [10]. However, these standard human brain imaging modalities are unable to provide direct and real-time feedback on spatial distribution and dynamic changes of DBS contact currents. There remains an urgent need of mapping and evaluating DBS contact currents to guide the lead direction and DBS regulation.

Acoustoelectric brain imaging (AEBI) is an emerging neuroimaging method that directly maps biological current density distribution by modulating brain tissue resistivity with focused ultrasound (FUS) [11], [12]. During ultrasound propagating in the brain tissue, local pressure changes cause periodic mechanical compression and expansion in the focused area. This small elastic deformation induces change in resistivity. The mechanism and methods of AEBI have been fully validated through experiments in previous research [13], [14], [15], [16], [17], [18]. Recently, researchers have advanced AEBI in different ways and made good progress. Some studies concentrated on optimizing AEBI hardware system. A custom ultrasound array was designed for AEBI with electronic

beam-steering through the human skull [19]. Then, a mobile AEBI platform was developed to map rat brain activity for easy transportation and adjustment [20]. In addition, some studies combined AEBI with specific brain disease diagnosis and treatment. For mapping deep dipole during epilepsy, AEBI showed much better resolution and accuracy [21]. Meanwhile, researchers investigated AEBI as a promising method for noninvasively imaging currents generated by DBS leads [22], [23]. It has been demonstrated that AEBI can map DBS currents inside human skulls submerged in 0.9% NaCl solution [24], [25]. Besides, we have demonstrated that the pulse repetition frequency (PRF) of FUS is capable of encoding electroencephalography (EEG) signal and decoding AE signal and proved its feasibility through *in vivo* rat brain AEBI experiments [26], [27], [28], [29], [30], [31]. Furtherly, based on PRF, living rat steady-state visual evoked potentials activation was mapped and the AE signal processing network of the rat brain was revealed [32], [33], [34], [35]. The above studies made important contributions to optimize AEBI imaging method for further clinical application.

Mapping brain current density by AEBI makes the spatial distribution and dynamic changes of DBS lead become observable and quantifiable. It worth noting that DBS has complex current parameters including stimulation amplitude, stimulation frequency, stimulation waveform, stimulation pulse duration and temporal pattern of stimulation, which are closely related to artificial activation of the nervous system [36], [37]. The temporal pattern of stimulation can influence the clinical outcome after DBS, particularly in Parkinson disease [37]. As a function of time, the stimulation waveform can influence the number and type of activated neural elements and waveforms or pulses can be repeated at various inter-pulse intervals to create a stimulation pattern [38]. The stimulation frequency and amplitude are common parameters in closed-loop DBS [39]. To further explore the potential of DBS visualization by AEBI, this study investigates *in vivo* AEBI of DBS currents with different stimulation parameters for the first time.

In this work, we extend AEBI to the imaging of *in vivo* DBS current distribution in living rat brains and provide a proof for the feasibility of characterizing different DBS currents of the brain. The main contributions of this study are as follows. Living rat brain AEBI experiments are performed with different DBS currents, including stimulation time pattern, stimulation waveform, stimulation frequency and stimulation amplitude. The AEBI images are drawn for each type DBS current and the imaging performance is evaluated. Specifically, we show that the decoded AE signal is correlated with the DBS current and explore its potential for characterizing of different DBS currents from multiple perspectives.

II. THEORY

AE effect is the physical foundation of AEBI. The FUS propagating wave causes acoustic pressure change ΔP which modifies the medium's initial resistivity ρ_0 and causes resistivity change $\Delta \rho$ [40], [41]. It follows the equation

$$\Delta \rho = -\rho_0 K \Delta P \qquad (1)$$

where K is a material-specific interaction constant which is of the order of 10^{-9} Pa^{-1} in 0.9% NaCl. As FUS transmits a resistivity medium, the resistivity distribution becomes

$$\rho = \rho_0 - \rho_0 K \Delta P \qquad (2)$$

A pair of electrodes is called a lead. According to the lead filed theory, the voltage U_i measured by lead i is

$$U_i = \iiint \rho(\tilde{J}_i^L \bullet J^I) dx dy dz \qquad (3)$$

where J^I is the current source and $\tilde{J}_i^L$ is the corresponding lead field [42]. According to (2) and (3), when FUS passes through the biological medium, the U_i can be mathematically expressed as [30]

$$U_i = U_i^{LF} + U_i^{AE} \qquad (4)$$

$$U_i^{LF} = \iiint \rho_0(\tilde{J}_i^L \bullet J^I) dx dy dz \qquad (5)$$

$$U_i^{AE} = \iiint (-\rho_0 K \Delta P)(\tilde{J}_i^L \bullet J^I) dx dy dz \qquad (6)$$

The measured voltage U_i is the summation of U_i^{LF} and U_i^{AE}. U_i^{LF} is the low frequency EEG signal produced by J^I. U_i^{AE} is the high frequency AE signal which is band-pass filtered by ultrasound center frequency or PRF in the FUS irradiated medium. So that, U_i^{LF} and U_i^{AE} can be extracted by different frequency bands [15]. According to (6), the AE signal is proportional to current density and sensitive to the current flow direction [13], [43]. Therefore, with the known focal spot and mm-level spatial resolution, AE signals can be acquired by FUS scanning the region of interest and then used to map current densities.

III. METHODS

A. Animals and Ethics Statement

AEBI of DBS currents were tested in sixteen Wistar rats weighed 260-320g who were maintained under standard housing conditions at a constant temperature and 12h reversed light-dark cycle. In each experiment, one rat was anesthetized with 30% urethane (4-5ml/kg) and placed on a stereotaxic device. This study was approved by the Animal Research Ethics Committee of Tianjin University.

B. Experiment Setup

The experimental setup is schematically shown in Fig. 1 (a), which consists of a concentric bipolar platinum-iridium electrode (diameter 40 μm) for DBS, a function generator (DG4162, RIGOL, CN), a FUS transducer (A303S, center frequency 1 MHz, PRF 1631 Hz, focal length 25 mm, Olympus, USA), a pulse transmitter (5077PR, Olympus, USA), a data acquisition system (SynAmps2, Neuroscan, USA) and rats. Fig. 1 (b) and (c) display the experimental scene, electrode locations and FUS focal spots. The lateral hypothalamic area (LH) was selected as the stimulating brain area which was a potential DBS target for coma arousal caused by traumatic brain injury [44]. As shown in Fig. 1 (b), taking bregma as the origin, the DBS electrode were inserted into LH (-2 mm,
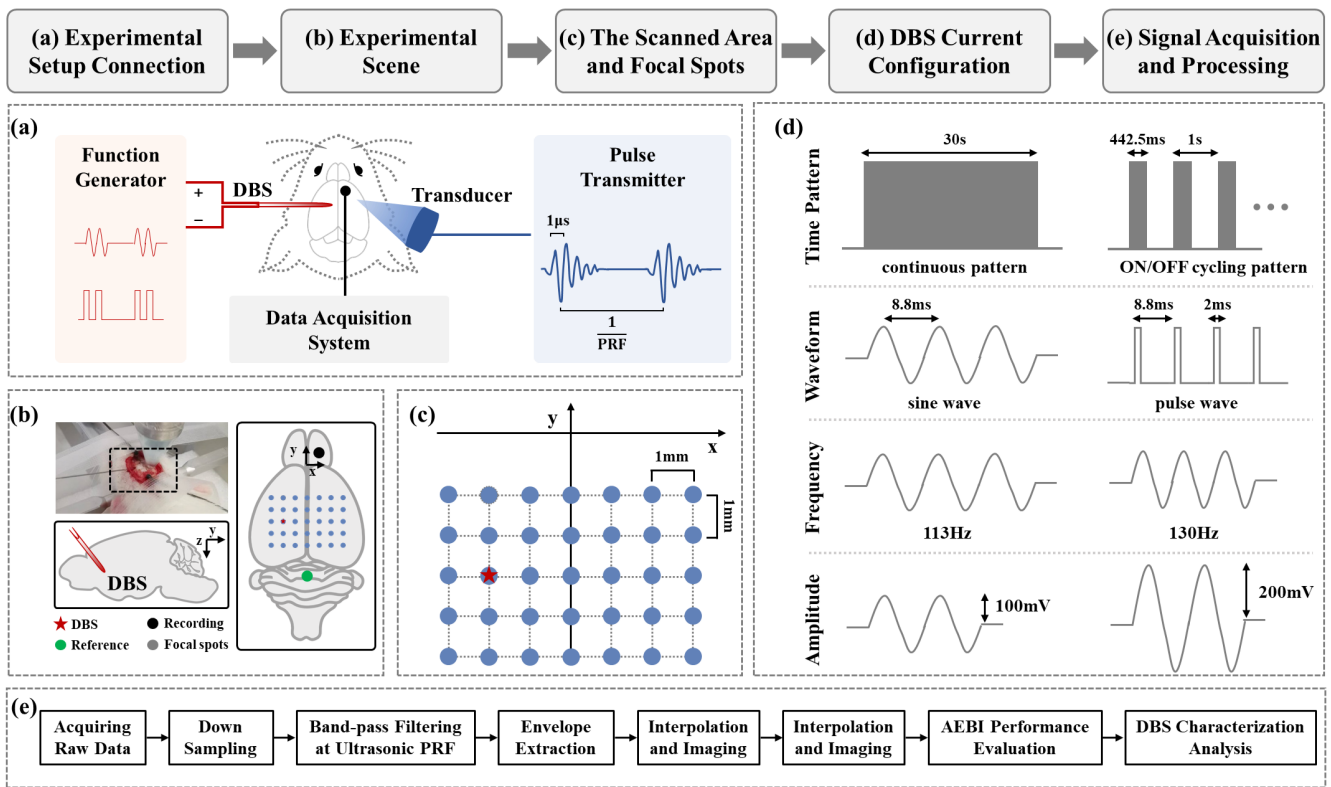
Fig. 1. Schematic diagram of the experimental design. (a) Schematic diagram of the experimental setup connection. (b) The experimental scene, and the position diagram of electrodes and focal spots in the AEBI experiment. (c) The scanned area and focal spots in the AEBI experiment. Along the x-direction, transducer scanned 6 mm (x = −3∼3mm), covering seven focal spots totally. Along the y-direction, it scanned 4mm (y = −2∼−6mm), generating six focal spots in total. (d) Schematic diagram of the DBS current configuration, including stimulating time pattern, waveform, frequency and amplitude. (e) Signal acquisition and processing flow.

−4 mm, −8 mm) in accordance with The Rat Brain in Stereotaxic Coordinates 6th. The cylindrical non-invasive electrodes (Ag/AgCl, diameter 1.0 mm) were placed on the skull surface to record EEG signal and AE signal. The recording electrode was placed at position (1 mm, 1 mm) which did not affect the scanning brain area. The reference electrode was located on the cerebellar (0 mm, −10.4 mm) where the active state was relatively weak and stable. The tail was chosen as the ground.

Connected to a stepper motor, the FUS transducer scanned around the DBS contact on x-y plane which was called C-scan in ultrasound imaging. As displayed in Fig. 1 (c), the size of the scan area was 6 mm × 4 mm with 1 mm step. The size of each focal spot was 2.8 mm laterally when ultrasound pressure decreased 3 dB. When the FUS transducer focused at each focal spot, the AE signal was recorded simultaneously.

C. DBS Configuration and Signal Acquisition

Fig. 1(d) shows the DBS current configuration used in this study, including time pattern of stimulation, stimulation waveform, stimulation frequency and stimulation amplitude. For the time pattern of stimulation, continuous and ON/OFF cycling stimulation were performed respectively in AEBI experiments which total duration were both 30s for each focal spot. For the DBS stimulation waveform, a sine wave (cycle time: 8.8ms) and a more realistic positive pulse (cycle time: 8.8ms, pulse width: 2 ms) were tested for AEBI. For the different frequencies, a 113 Hz and 130 Hz sine stimulation

TABLE I
DBS CURRENT PARAMETERS AND CONTACT POSITIONS

PARAMETERS		Location (mm)
Time Pattern	Continuous	(-1, -4)
	ON/OFF cycling	(-2, -4)
Waveform	Sine wave	(-1, -4)
	Pulse wave	(0, -3)
Frequency	113 Hz	(-1, -4)
	130 Hz	(-2, -4)
Amplitude	100 mV	(-2, -4)
	200 mV	(-2, -4)

were respectively adopted in AEBI experiments. For the DBS stimulation amplitude, a 100 mV and 200 mV (peak value) sine wave stimulation were respectively used in AEBI experiments. The specific DBS current parameters and contact positions are listed in Table I. To test the AEBI's ability to distinguish small positional changes, the locations of DBS contact were changed slightly within LH.

In the AEBI experiment, two rats were used for each DBS configuration respectively. 30 s voltage signal of each position was recorded simultaneously when FUS transducer scanning on the corresponding focal spot. The voltage signals generated by DBS stimulation were acquired by a SynAmps2 system with a 20 kHz sampling rate. All acquisitions were performed at spatial peak temporal average intensity (I_{spta})

of 42.8 mW/cm^2 and mechanical index (MI) of 0.78 which were within Food and Drug Administration recommendations to limit tissue damage.

D. Image Protocol

In this study, PRF was used to extract AE signal from raw signal which was validated in previous work [26], [27], [28], [29], [30], [31]. The voltage signals acquired at each focal spot initially were used as the raw data and was first down sampled at 5000 Hz. Then, the preprocessed signals were band-pass filtered from PRF-50Hz to PRF+50Hz with Butterworth filter to retain the high frequency component at the ultrasonic PRF (AE signal). The envelope of the AE signal was extracted by Hilbert transform which indicated the magnitude of local current densities. After 100-150 Hz band-pass filtering of the envelope signal, the decoded AE signal was obtained. To map DBS current density, the averaged value of envelope signal was taken as AE signal intensity for each focal spot. Then the matrix of AE signal intensity could be formed according to the preset coordinate of focal spots. Finally, the AE intensity matrix was interpolated at 0.01 mm interval between the adjacent focal points to reconstruct AEBI image. The specific flow schematic is shown in Fig. 1(e).

E. Evaluation Indicators

To evaluate AEBI image performance, the spatiotemporal resolution and imaging signal-to-noise ratio (SNR) were quantified. Spatial lateral (axial) resolution was defined as the width at 3 dB attenuation of AE signal peak which was measured along the x or y direction [24], [28], [34], [45]. The SNR was calculated in decibels according to (7). The *Signal* was the AE signal amplitude at the DBS electrode position and the *Noise* was the mean value of the AE signal amplitude at 20 edge locations [28].

$$SNR = 20 \times log_{10}(Signal/Noise) \qquad (7)$$

To evaluate the feasibility of DBS characterization by decoded AE signal, the AE signal responses were discussed in time and frequency domain according to each DBS current configuration. In condition of different DBS time patterns, the averaged power variation of signal in time-frequency domain was calculated by short-time Fourier transform [46]. In condition of different DBS waveforms, the correlation analysis of decoded AE signal and DBS current was employed by the Pearson correlation test to evaluate the consistent degree in time domain [47]. The width of sliding window was 5 ms. In condition of different DBS frequencies, the frequency-amplitude spectrum of decoded AE signal was calculated by fast Fourier transform (FFT). Based on frequency-amplitude spectrum, FFT-SNR was defined as the ratio of FFT amplitude to the mean value of the 10 neighboring frequencies [48]. In condition of different DBS amplitudes, the amplitudes of AE signal at all sample points were compared by paired samples t-test.
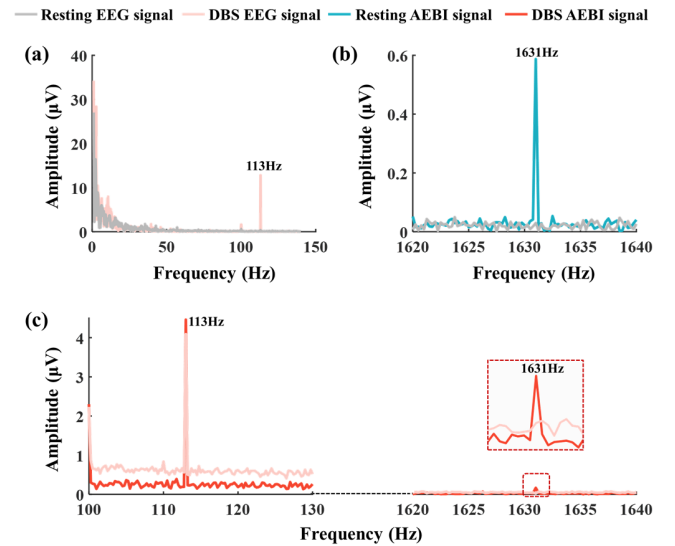

Fig. 2. Recorded signal spectrum. (a) is the spectrum of resting EEG signal and DBS EEG signal. (b) is the spectrum of resting EEG signal and resting AEBI signal. (c) is the spectrum of DBS AEBI signal and DBS EEG signal, red dashed box magnifies the comparison at 1631 Hz. (Resting EEG signal: gray curve; DBS EEG signal: pink curve; Resting AEBI signal: green curve; DBS AEBI signal: red curve).

IV. RESULTS

A. Analysis of Recorded Signals

For one rat, the spectrum of resting EEG signal, DBS EEG signal, resting AEBI signal and DBS AEBI signal are displayed in Fig 2. Fig. 2(a) shows the spectrum of EEG signal with and without DBS stimulation in a low frequency range. There is an obvious peak at the 113 Hz DBS frequency of DBS EEG signal, while no clear peak can be observed in the resting EEG spectrum. Fig. 2(b) displays the high frequency band spectrum of signal with and without FUS encoding. In comparison with resting EEG signal, resting AEBI signal has an obvious peak at 1631 Hz which is exactly the PRF of FUS. The spectrum of DBS EEG signal and DBS AEBI signal are displayed in Fig. 2(c). In the high-frequency band, DBS AEBI signal contains the 1631 Hz frequency of FUS and DBS EEG signal without FUS encoding has no specific frequency response. In the low-frequency band, the peak of DBS AEBI spectrum is consistent with DBS EEG spectrum. These results proves that the low frequency component of the AEBI signal and EEG signal are consistent. Simultaneously, a significant AE signal at PRF (high frequency component) can be obtained with AEBI.

B. AEBI and Decoded AE Signal of DBS Current With Different Time Patterns

1) AEBI Images: Fig. 3 displays AEBI images of DBS current with different temporal stimulation patterns (continuous and ON/OFF cycling). Under continuous DBS stimulation, Fig. 3(a) shows the AEBI images taken for 1s duration marked "A" (0-1s), "B" (1-2s), "C" (2-3s) and "D" (3-4s). It can be seen from Fig. 3(a) that, the position of DBS contact can be located at ($x = -1$, $y = -4$) with high current density observed in each 1s duration AEBI image, which is consistent

with the set position of DBS electrode. Under ON/OFF cycling stimulation pattern, a sequence of AEBI images during DBS cycle ("E", "F", "G", "H") are shown in Fig. 3 (b). During ON state of DBS stimulation, illustrated by 442.5 ms duration "F" and "H", the high intensity current density appears at ($x = -2$, $y = -4$) where the DBS contact is located. The following AEBI images of "E" and "G" show a current density distribution when DBS current turns to OFF state. Quantitatively, the normalized current density along twelve white dashed-lines (L_{xA}, L_{xB}, L_{xC}, L_{xD}, L_{xF}, L_{xH}, L_{yA}, L_{yB}, L_{yC}, L_{yD}, L_{yF}, L_{yH}) in "A", "B", "C", "D", "F" and "H" are shown in Fig. 3 (c) and (d). For continuous DBS shown in Fig. 3 (c), the contact width of the -3 dB peak is 4 mm, 1.69 mm, 3.33 mm and 2.40 mm respectively along the x direction (lateral resolution). Along the y direction, the axial resolution is 1.70 mm, 1.57 mm, 1.33 mm and 1.46 mm respectively. For ON/OFF cycling DBS shown in Fig. 3 (d), the lateral resolution is 1.46 mm and 1.45 mm respectively. Along the y direction, the axial resolution is 1.52 mm and 1.55 mm respectively. These results suggest that, with a millimeter-level (< 2 mm) spatial resolution, the AEBI can be used for localizing DBS contact and mapping current density for varying time patterns.

2) Time-Frequency Spectra Analysis: The time-frequency spectrogram of decoded AE signal at DBS contact is analyzed to describe the characteristic of continuous and ON/OFF cycling time pattern. The time-frequency spectra are calculated at two timescales (1 s and 5 s) for continuous and ON/OFF cycling patterns respectively as shown in Fig. 4. It can be seen from Fig. 4(a) that, during 1s or 5 s of continuous DBS stimulation, the time-frequency spectrogram of decoded AE signal shows a clear continuous power enhancement at 113 Hz which is consistent with DBS stimulus frequency. As exhibited in Fig. 4(b), in 1 s duration of ON/OFF cycling DBS, a clear power enhancement of decoded AE signal occurs at 113 Hz during ON state (from 0.3 s to 0.7425 s). For a larger timescale of 5 s duration, a power enhancement of decoded AE signal can be observed in turn. Besides, during the DBS OFF state, no significant enhancement can be seen in the time-frequency spectrogram of the decoded AE signal. These results indicate that the decoded AE signal has the same power change in time-frequency domain as the corresponding DBS time pattern.

C. AEBI and Decoded AE Signal of DBS Current With Different Waveforms

1) AEBI Images: Fig.5(a) and Fig.5(c) display AEBI images of the DBS current with sine wave and pulse wave. Fig.5(a) shows a sequence of AEBI images at five time points ''A-E'' during one sine wave DBS cycle. At the position of DBS contact ($x = -1$, $y = -4$), the strongest AE signal is observed at time point "B" and the weakest AE signal occurs at time point "D", which are consistent with the dynamic activation pattern of the sine wave DBS current. For the pulse wave stimulation, five AEBI images at time point "F-J" during one cycle are illustrated in Fig. 5(c). It can be seen at time point "I" that, the position of DBS contact can be located at ($x = 0$, $y = -3$) with the strongest current density observed

within 2 ms pulse width. In addition, a relatively low current density also can be mapped by AEBI on the rising (time point "H") and descending (time point "J") edge of the stimulus pulse, while there is no clear AE signal at time point "F" and "G". These results suggest that, with ms-level temporal resolution and mm-level spatial resolution, AEBI is capable of non-invasively localizing the DBS contact and visualizing the stimulus state of different current waveforms.

2) Timing Analysis: To further characterize DBS current in time domain, the waveform of decoded AE signal at the contact and the responding DBS current are exhibited in Fig. 5(b) and (d). For the sine DBS as shown in Fig. 5(b), 50 ms of the decoded AE signal and stimulus signal are displayed respectively which are positively correlated in both amplitude and phase. Described by the color map of correlation on the top, the decoded AE has a significant correlation with the sine DBS current ($r = 0.8442$, $p < 0.001$). For the pulse DBS as shown in Fig. 5(d), the decoded AE signal and stimulus signal are also positively correlated in amplitude and phase. And there is a significant positive relationship between the waveforms of decoded AE signal and pulse DBS signal: $r = 0.7941$, $p < 0.001$. These experimental results validate that the decoded AE signal can be used to characterize DBS currents with different waveforms.

D. AEBI and Decoded AE Signal of DBS Current With Different Frequencies

Fig. 6 shows AEBI images and decoded AE signal spectrum of the 113Hz and 130 Hz DBS currents. As exhibited in Fig. 6(a), the DBS contact can be located at position ($x = -1$, $y = -4$) with an obvious high current density. In addition, the decoded AE signal spectrum at DBS contact ($x = -1$, $y = -4$), position A ($x = -2$, $y = -4$), position B ($x = -1$, $y = -2$), position C ($x = 2$, $y = -4$) and position D ($x = -1$, $y = -5$) are displayed on the right panel. When transducer focused at the DBS contact, there is a high amplitude response at DBS stimulus frequency 113 Hz and it reaches 11.9 dB FFT-SNR. It worth noting that, at other spots such as A, B, C, and D, there is no amplitude response can be observed at a certain frequency. As shown in Fig. 6(b), with a high current density, the DBS contact is located at ($x = -2$, $y = -4$). It can be observed in its spectrogram that, at DBS contact ($x = -2$, $y = -4$), a high decoded AE amplitude response of 130 Hz is very clear visible with 14.1 dB FFT-SNR which is consistent with the DBS stimulus. Also, the amplitude response at 130 Hz disappears when transducer focuses on position E, F, G and H. These results indicate that decoded AE signal is capable of characterizing DBS currents with different frequencies.

E. AEBI and Decoded AE Signal of DBS Current With Different Amplitudes

Fig. 7 shows the AEBI experimental results of 100 mV and 200 mV DBS currents. Fig. 7(a) and (b) display the AE signal amplitude matrix and AEBI image of 100 mV DBS respectively. Fig. 7(c) and (d) present the AE signal amplitude matrix and AEBI image of the 200 mV DBS respectively. Fig. 7(e) shows the AE signal amplitude comparation between
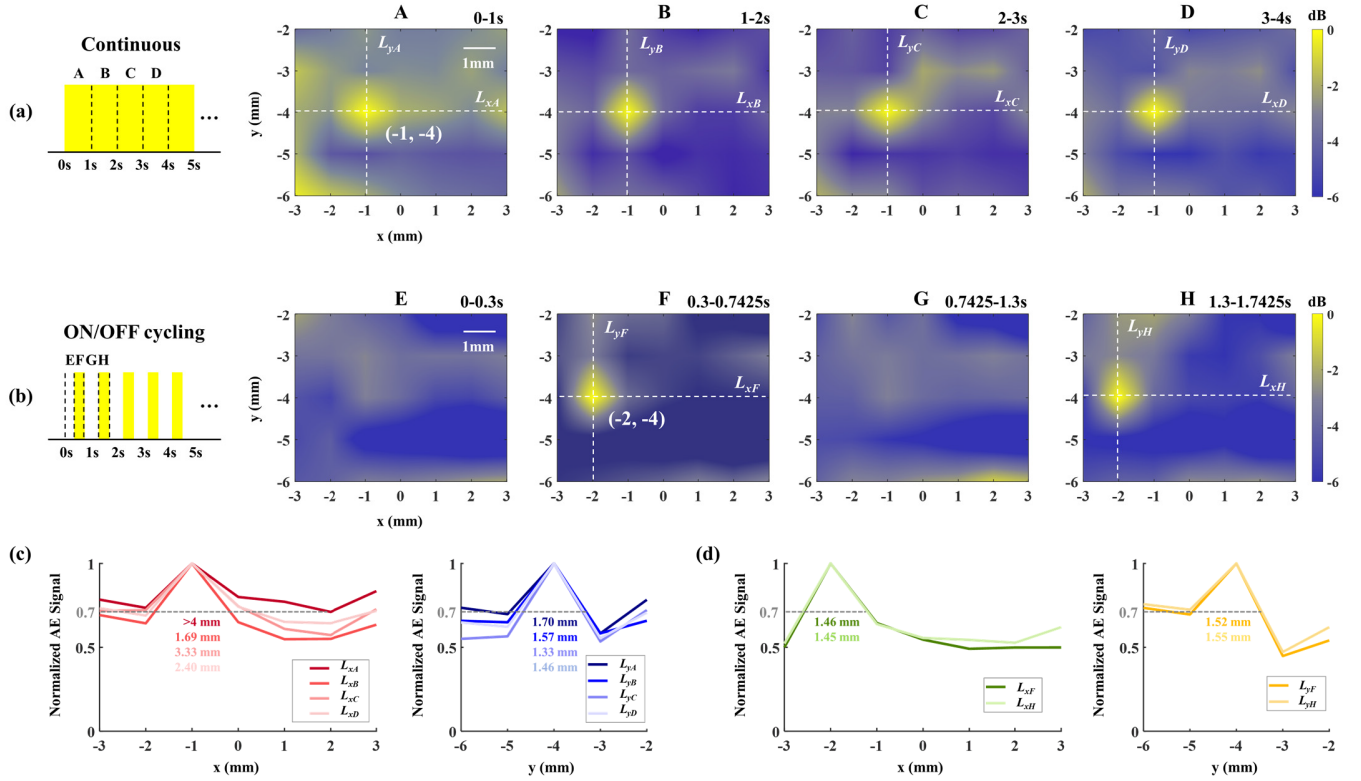
Fig. 3.   AEBI images of the DBS current with different time patterns. (a) AEBI images of the continuous DBS stimulation. (b) AEBI images of the ON/OFF cycling DBS stimulation. (c) The normalized current density along the eight white dashed-lines (L_{xA}, L_{xB}, L_{xC}, L_{xD}, L_{yA}, L_{yB}, L_{yC}, L_{yD}) in the continuous DBS AEBI images. (d) The normalized current density along the four white dashed-lines (L_{xF}, L_{xH}, L_{yF}, L_{yH}◁ in the ON/OFF cycling DBS AEBI images.
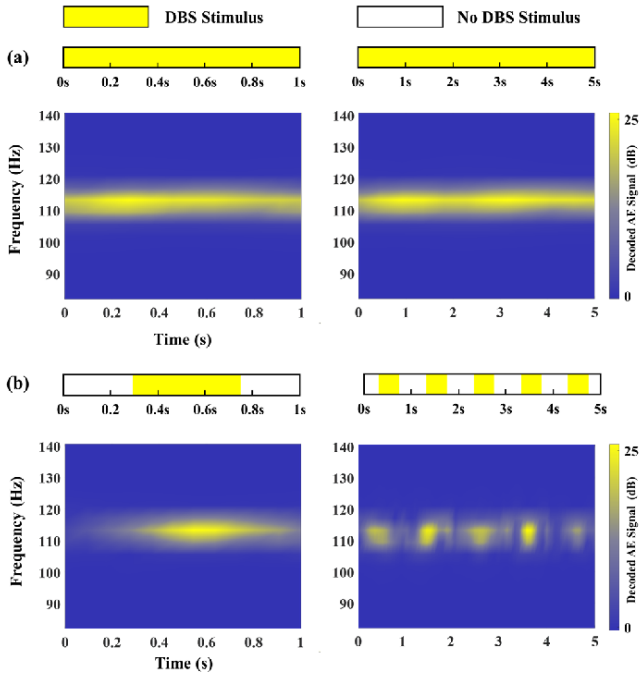

Fig. 4.   Time-frequency spectrograms of decoded AE signal at the DBS contact with continuous (a) and ON/OFF cycling (b) time pattern. (a) and (b) both display the time-frequency spectra in 1-second and 5-second period. The color bar indicates the dB-value of energy change.

100 mV and 200 mV DBS current for all focal spots. As shown in Fig. 7, the position of 100 mV and 200 mV DBS

currents both can be located at ($x = -2$, $y = -4$) which are agreed with the set position of DBS electrodes. Within the same quantification range of AE signal amplitude, the AEBI image of 200 mV DBS shows a relatively higher spatial resolution than that of 100 mV DBS. In addition, the AE signal amplitude of 200 mV DBS is stronger than that of 100 mV DBS at each focal spot. Their averaged amplitudes are respectively 2.16 μV (100 mV DBS) and 4.42 μV (200 mV DBS). According to the result of paired-samples t-test, there is a significant difference between AE signal amplitude of 100 mV and 200 mV DBS stimulus: $t(34) = -18.466$, $p < 0.001$. These results demonstrate that AEBI is capable of mapping DBS current density and characterizing DBS currents with different amplitudes.

V. DISCUSSION

According to the typical DBS stimulus parameters, we designed four types of DBS currents (time pattern, waveform, frequency, and amplitude) to explore the potential of *in vivo* DBS visualization using AEBI. As results, *in vivo* transcranial AEBI can accurately localize DBS contact current region which is consistent with the actual position of DBS electrode, reaching a spatiotemporal resolution of 2.2 ms and 1.46 mm, and 11.2 dB SNR. Furtherly, the decoded AE signals are analysed in time-frequency domain, spatial distribution, and amplitude comparison for each DBS current type. It is demonstrated that the decoded AE signal at the DBS contact
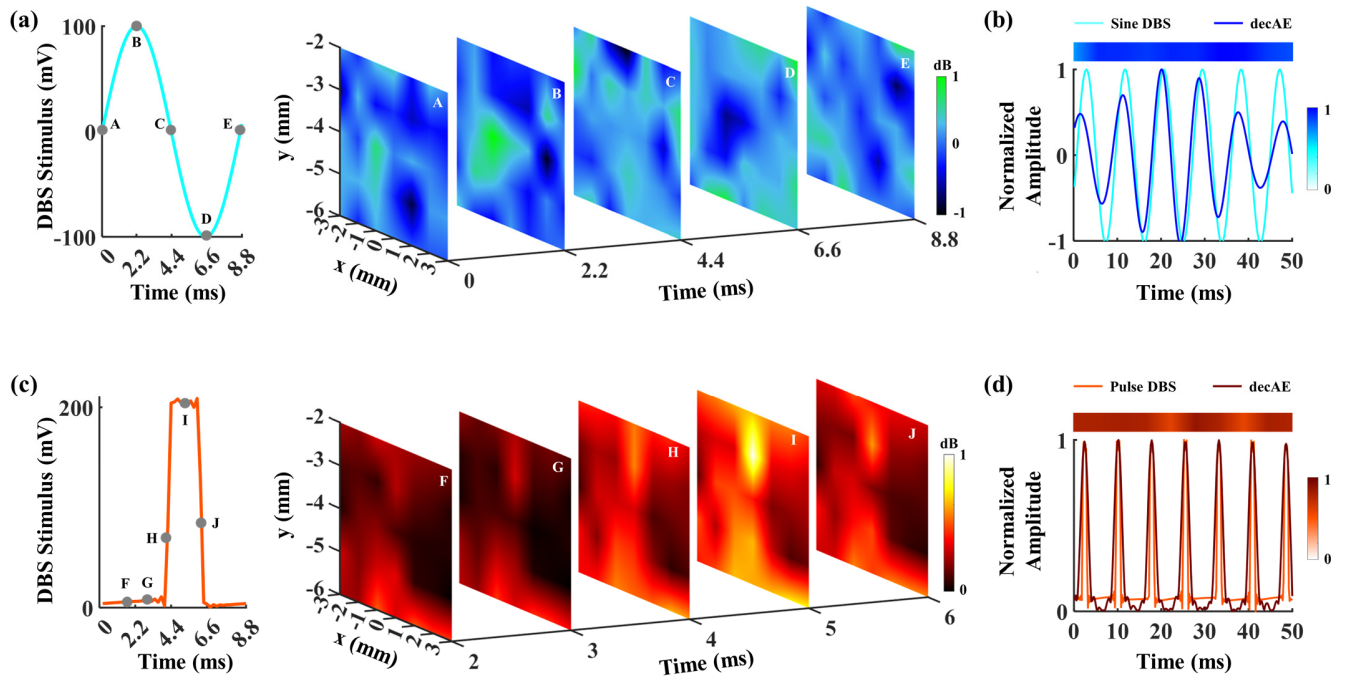
Fig. 5. AEBI images and decoded AE signal waveform of DBS currents with different waveforms. (a) Sine wave DBS: AEBI obtained during one cycle with single AEBI images at the different time-points marked by A, B, C, D and E. (b) Normalized sine DBS current and decoded AE signal. The correlation between decoded AE signal and DBS current is indicated by the color map along time axis whose value is referring to the color bar on the right. (c) Pulse wave DBS: AEBI obtained during one cycle with single AEBI images at the different time-points marked by F, G, H, I and J. (d) Normalized pulse DBS current and decoded AE signal. The correlation between decoded AE signal and DBS current is indicated by the color map along time axis whose value is referring to the color bar on the right. (decAE is short for decoded AE).
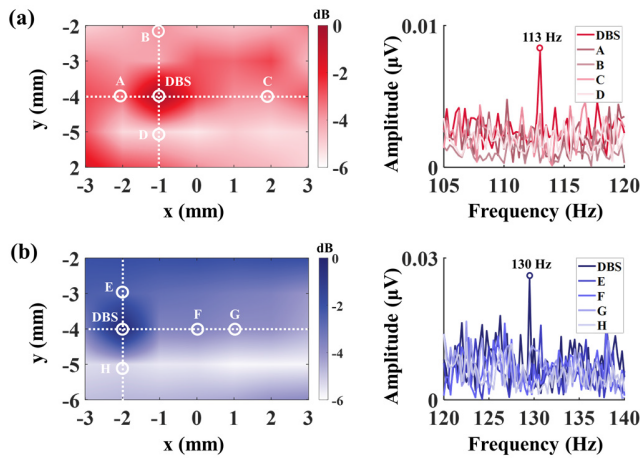

Fig. 6. AEBI images and decoded AE spectrograms of DBS current with different frequencies. (a) The AEBI image of 113 Hz DBS current and the decoded AE spectrum at position DBS and A-D. (b) The AEBI image of the 130 Hz DBS current and the decoded AE spectrum at position DBS and E-H.
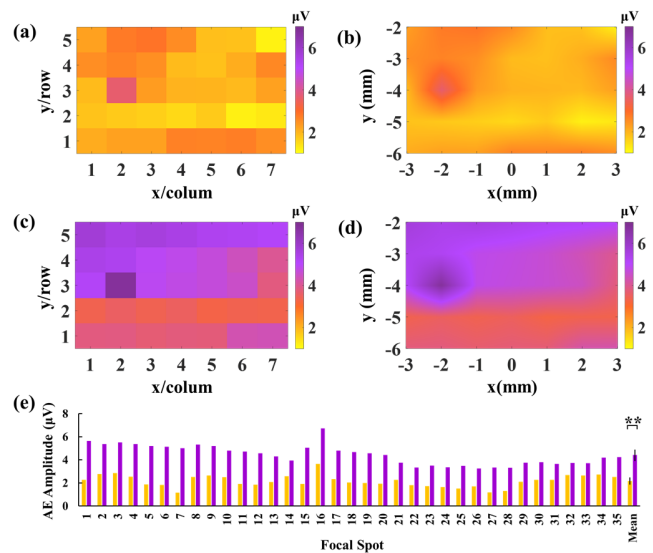

Fig. 7. AEBI images and AE amplitude comparison of DBS current with different amplitudes. (a) AE signal matrix of 100 mV DBS current. (b) AE signal map of 100 mV DBS current. (c) AE signal matrix of 200 mV DBS current. (d) AE signal map of 200 mV DBS current. The color bar indicates the μV-value of AE signal change.

position can be used to effectively describe the corresponding DBS current characteristics from multiple perspectives.

It is interesting that we achieved *in vivo* DBS current localization in rats under four types of DBS currents using only one pair of recording electrodes placed on the skull. It avoids the implanting electrodes into brain and localizes DBS current as well. Different from conventional method of DBS electrode localization and lead reconstruction based on MRI and CT, AEBI can localize the DBS contact and identify

current pattern changes by measuring AE signal which is an electrical signal and directly proportional to the current density and direction [25]. For different DBS time patterns, the AEBI images and time-frequency spectra of decoded AE signals with continuous DBS both show a continuously stable AE intensity response. The AEBI images and time-frequency spectra of
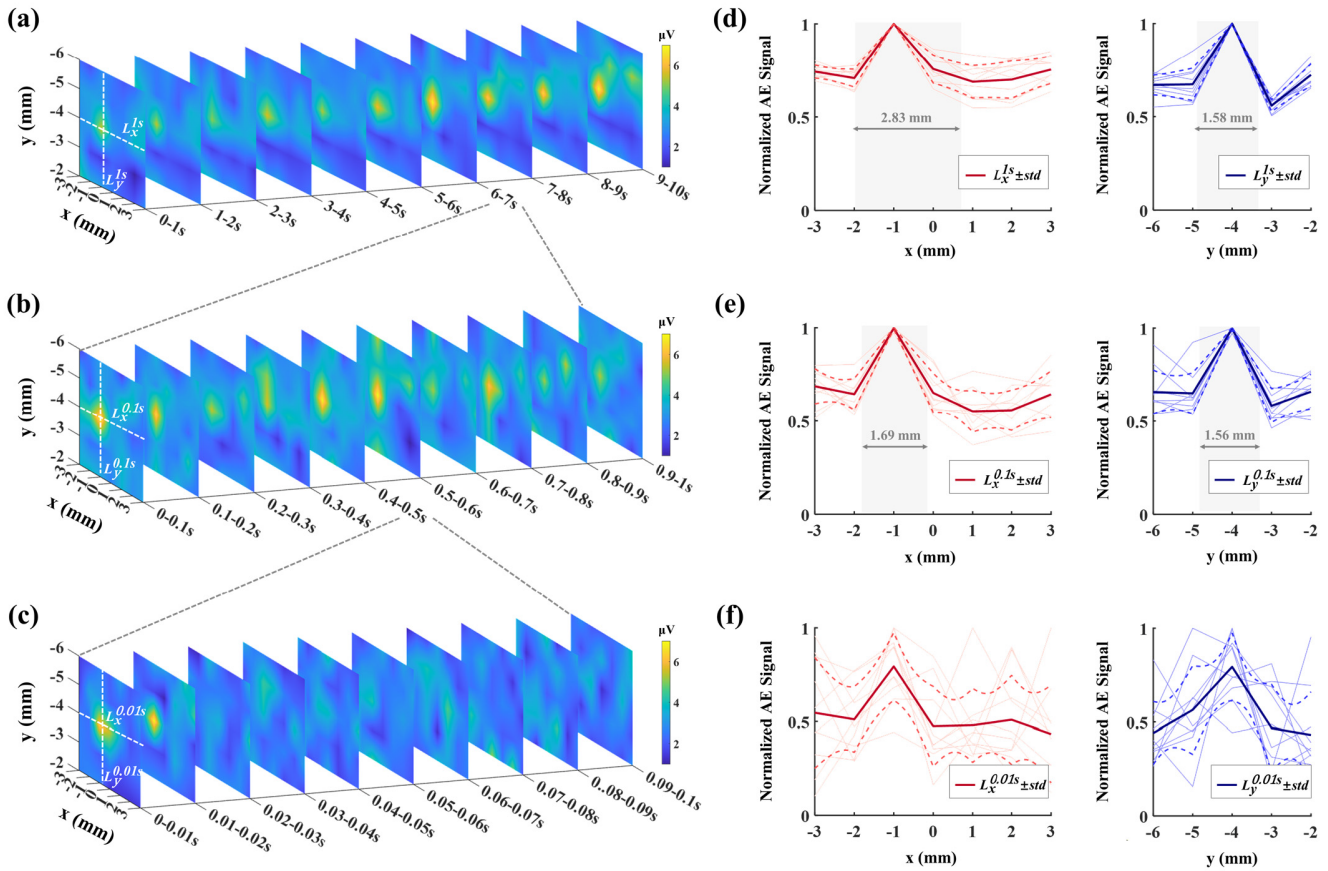
Fig. 8.   AEBI images and spatial resolution within 1 s, 100 ms and 10 ms. (a) Single AEBI images within 1 s during the continues ten seconds. (b) Single AEBI images within 100 ms during the continues 1 seconds. (c) Single AEBI images within 10 s during the continues 0.1 seconds. (d) Normalized AE intensity profiles along the white dashed lines of each 1 s AEBI image. (e) Normalized AE intensity profiles along the white dashed-lines of each 100 ms AEBI image. (f) Normalized AE intensity profiles along the white dashed-lines of each 10 ms AEBI image. (a)-(c): The color bar indicates the μV-value of AE signal. (d)-(f): Light red and light blue solid line indicates AE intensity profile of each AEBI image shown in (a)-(c). Red and blue solid line indicates mean value of AE intensity variation. Red and blue dashed lines indicate the corresponding standard deviation. The overlapped grey rectangle indicates the averaged contact width of the -3 dB peak of the AE signal.

decoded AE signals with ON/OFF cycling DBS can reflect the corresponding cyclic change process of current densities. For different DBS waveforms, frequencies, and amplitudes, their AEBI images and decoded AE signal characteristics (timing correlation, spectrum, and amplitude) all have differences due to their different current sources. This further confirms the brain imaging feasibility of AEBI.

To further discuss AEBI performance in spatiotemporal resolution, we calculated AEBI at different timescales for one rat under continuous sine DBS current stimulus. The AEBI images of 1 s, 100 ms and 10 ms are respectively shown in Fig. 8 (a)-(c). With an obvious strong signals observed at position ($x = -1$, $y = -4$), a consistent DBS current mapping are presented for the three timescales. In addition, Fig. 8 (d)-(f) show the AE intensity profile along the white dashed-line L_x and L_y for each corresponding AEBI image. The bold solid lines represent the averaged AE intensity of 10 images and the dashed lines represent the corresponding standard deviation.

As shown in Fig. 8 (a), with 1 s timescale, the DBS contact can be located clearly for each AEBI image. The AE intensity profile of each 1 s AEBI image are drawn by the light red and light blue solid lines in Fig. 8 (d). For each 1 s duration, there is an obviously consistent AE intensity variation with mean (red and blue solid lines) and standard

deviation (red and blue dashed lines): x direction 0.767 ± 0.059, y direction 0.732 ± 0.043. Its averaged lateral and axial resolution are 2.83 mm and 1.58 mm indicating by the overlapped grey rectangles. Dividing AEBI image of 6-7 s into ten equal periods, as displayed in Fig. 8 (b), the DBS contact can be mainly located in most AEBI images within 100 ms. As shown in Fig. 8 (e), the AE intensity trend during each 100 ms seems to be a little disperse with mean and standard deviation (x direction: 0.678 ± 0.077, y direction: 0.722 ± 0.072). Its averaged lateral and axial resolution are 1.69 mm and 1.56 mm. Furthermore, the AEBI image of 0.4-0.5 s is divided into ten equal periods for shorter timescale. With 10 ms timescale, it is difficult to identify the DBS contact in AEBI images from 0.02 s to 1 s. With mean and standard deviation of 0.543 ± 0.179 along the x direction and 0.565 ± 0.162 along the y direction, there is a greater difference in the AE intensity variation between each 10 ms AEBI image.

The above analysis indicates that as timescale shortens, the spatial resolution may be unstable between AEBI images. It should be noted that these transient AEBI images are formed with the single-sample AE signals, causing a different degrees of noise interference. For very short timescale such as 10 ms in this study, the noise interference may be reduced by averaging AE signal across stimulating trials to improve the SNR, and

then the stability of spatial resolution can be enhanced to present a high performance over time [32].

In this study, only one DBS contact spreading different currents was taken as the imaging target, and thus, the DBS stimulus needs to be designed more closely to actual clinical application. For examples, selection of the active electrode contacts (or electrode geometry) and current direction should be considered for a directional DBS leads with multi contacts which can achieve a precise treatment [49]. Furthermore, it is necessary to optimize spatially encoding and decoding methods by FUS for complex imaging target [50]. The stereotaxic coordinate and the known electrode positions are used as a reference to evaluate the AEBI localization. The detection of electrocorticography can be considered as reference for AEBI location in the next study.

By directly localizing DBS contact and mapping its current, AEBI may help to enhance DBS electrodes placement accuracy and guide DBS current regulation. With high spatiotemporal resolution, AEBI has great potential to develop into a noninvasive DBS current real-time monitoring technique, supporting visualization of DBS current spatial distribution and dynamic changes. More significantly, it is expected to establish a DBS current feedback pathway from electrophysiology, providing a novel direction for DBS closed-loop control research [51].

VI. Conclusion

In this study, *in vivo* transcranial AEBI of different DBS currents were achieved. It can locate the position of DBS contact with a mm-level spatial resolution (<2mm) and ms-level temporal resolution (<10ms). In addition, the decoded AE signal is capable of describing the corresponding DBS current characteristics and identifying current pattern changes. This study validates the feasibility of AEBI to detect *in vivo* DBS current and it is expected to develop into a noninvasive DBS current real-time monitoring technology with high spatiotemporal resolution.

References

[1] J. Frey et al., "Past, present, and future of deep brain stimulation: Hardware, software, imaging, physiology and novel approaches," *Frontiers Neurol.*, vol. 13, Mar. 2022, Art. no. 825178.

[2] J. K. Krauss et al., "Technology of deep brain stimulation: Current status and future directions," *Nature Rev. Neurol.*, vol. 17, no. 2, pp. 75–87, Feb. 2021.

[3] S. Negi, R. Bhandari, L. Rieth, R. Van Wagenen, and F. Solzbacher, "Neural electrode degradation from continuous electrical stimulation: Comparison of sputtered and activated iridium oxide," *J. Neurosci. Methods*, vol. 186, no. 1, pp. 8–17, Jan. 2010.

[4] D. Satzer, D. Lanctin, L. E. Eberly, and A. Abosch, "Variation in deep brain stimulation electrode impedance over years following electrode implantation," *Stereotactic Funct. Neurosurgery*, vol. 92, no. 2, pp. 94–102, Feb. 2014.

[5] G. Fernández-Pajarín et al., "Delayed complications of deep brain stimulation: 16-year experience in 249 patients," *Acta Neurochirurgica*, vol. 159, no. 9, pp. 1713–1719, Sep. 2017.

[6] T. A. Dembek et al., "Directional DBS leads show large deviations from their intended implantation orientation," *Parkinsonism Rel. Disorders*, vol. 67, pp. 117–121, Oct. 2019.

[7] A. Horn and A. A. Kühn, "Lead-DBS: A toolbox for deep brain stimulation electrode localizations and visualizations," *NeuroImage*, vol. 107, pp. 127–135, Feb. 2015.

[8] P. M. Lauro et al., "DBSproc: An open source process for DBS electrode localization and tractographic analysis," *Hum. Brain Mapping*, vol. 37, no. 1, pp. 422–433, Jan. 2016.

[9] M. Milchenko et al., "ESM-CT: A precise method for localization of DBS electrodes in CT images," *J. Neurosci. Methods*, vol. 308, pp. 366–376, Oct. 2018.

[10] U. Walter et al., "Magnetic resonance-transcranial ultrasound fusion imaging: A novel tool for brain electrode location," *Movement Disorders*, vol. 31, no. 3, pp. 302–309, Mar. 2016.

[11] B. He, "Focused ultrasound help realize high spatiotemporal brain imaging?—A concept on acousto-electrophysiological neuroimaging," *IEEE Trans. Biomed. Eneenring*, vol. 63, no. 12, pp. 2654–2656, Dec. 2016.

[12] H. Zhang et al., "Biological current source imaging method based on acoustoelectric effect: A systematic review," *Frontiers Neurosci.*, vol. 16, Jul. 2022, Art. no. 807376.

[13] B. Lavandier, J. Jossinet, and D. Cathignol, "Experimental measurement of the acousto-electric interaction signal in saline solution," *Ultrasonics*, vol. 38, no. 9, pp. 929–936, Sep. 2000.

[14] B. Lavandier, J. Jossinet, and D. Cathignol, "Quantitative assessment of ultrasound-induced resistance change in saline solution," *Med. Biol. Eng. Comput.*, vol. 38, no. 2, pp. 150–155, Mar. 2000.

[15] R. Olafsson, R. S. Witte, S.-W. Huang, and M. O'Donnell, "Ultrasound current source density imaging," *IEEE Trans. Biomed. Eng.*, vol. 55, no. 7, pp. 1840–1848, Jul. 2008.

[16] Y. Qin, Q. Li, P. Ingram, C. Barber, Z. Liu, and R. S. Witte, "Ultrasound current source density imaging of the cardiac activation wave using a clinical cardiac catheter," *IEEE Trans. Biomed. Eng.*, vol. 62, no. 1, pp. 241–247, Jan. 2015.

[17] A. Alvarez et al., "In vivo acoustoelectric imaging for high-resolution visualization of cardiac electric spatiotemporal dynamics," *Appl. Opt.*, vol. 59, no. 36, p. 11292, Dec. 2020.

[18] B. Berthon et al., "Mapping biological current densities with ultrafast acoustoelectric imaging: Application to the beating rat heart," *IEEE Trans. Med. Imag.*, vol. 38, no. 8, pp. 1852–1857, Aug. 2019.

[19] Y. Qin, P. Ingram, Z. Xu, M. O'Donnell, and R. S. Witte, "Performance of a transcranial U.S. Array designed for 4D acoustoelectric brain imaging in humans," in *Proc. IEEE Int. Ultrason. Symp. (IUS)*, Sep. 2017, pp. 1–4.

[20] A. Burton, C. A. Wilhite, T. K. Bera, P. Ingram, S. L. Cowen, and R. S. Witte, "Development of a mobile platform for acoustoelectric brain imaging in rats," in *Proc. IEEE Int. Ultrason. Symp. (IUS)*, Oct. 2018, pp. 1–4.

[21] A. Barragan et al., "Acoustoelectric imaging of deep dipoles in a human head phantom for guiding treatment of epilepsy," *J. Neural Eng.*, vol. 17, no. 5, Oct. 2020, Art. no. 056040.

[22] C. Preston, Y. Qin, P. Ingram, W. Kassof, A. Burton, and R. S. Witte, "Acoustoelectric imaging of time-varying current produced by a clinical deep brain stimulator," in *Proc. IEEE Int. Ultrason. Symp. (IUS)*, Sep. 2017, pp. 1–4.

[23] C. Preston, A. Alvarez, A. Barragan, W. S. Kasoff, and R. S. Witte, "Detecting deep brain stimulation currents with high resolution transcranial acoustoelectric imaging," in *Proc. IEEE Int. Ultrason. Symp. (IUS)*, Oct. 2019, pp. 2041–2044.

[24] C. Preston, W. S. Kasoff, and R. S. Witte, "Selective mapping of deep brain stimulation lead currents using acoustoelectric imaging," *Ultrasound Med. Biol.*, vol. 44, no. 11, pp. 2345–2357, Nov. 2018.

[25] C. Preston, A. M. Alvarez, A. Barragan, J. Becker, W. S. Kasoff, and R. S. Witte, "High resolution transcranial acoustoelectric imaging of current densities from a directional deep brain stimulator," *J. Neural Eng.*, vol. 17, no. 1, Feb. 2020, Art. no. 016074.

[26] Y. Zhou, X. Song, X. Chen, X. Zhao, Y. Ke, and D. Ming, "A source signal modulation mechanism with pulse focused ultrasound for acoustoelectric brain imaging," in *Proc. 9th Int. IEEE/EMBS Conf. Neural Eng. (NER)*, Mar. 2019, pp. 766–769.

[27] Y. Zhou, X. Song, Z. Wang, X. Zhao, X. Chen, and D. Ming, "Coding biological current source with pulsed ultrasound for acoustoelectric brain imaging: Application to vivo rat brain," *IEEE Access*, vol. 8, pp. 29586–29594, 2020.

[28] H. Zhang et al., "Experimental and simulation studies of localization and decoding of single and double dipoles," *J. Neural Eng.*, vol. 19, no. 2, May 2022, Art. no. 025002.

[29] X. Song, G. Han, Y. Zhou, M. Xu, M. Liu, and D. Ming, "A symmetrical sensor configuration for acoustoelectric brain imaging," *IEEE Sensors J.*, vol. 21, no. 20, pp. 22891–22898, Oct. 2021.

[30] Y. Zhou, X. Song, Z. Wang, F. He, and D. Ming, "Multisource acoustoelectric imaging with different current source features," *IEEE Trans. Instrum. Meas.*, vol. 70, pp. 1–9, 2021.

[31] X. Song, T. Wang, M. Su, X. Chen, X. Liu, and D. Ming, "An adaptive acoustoelectric signal decoding algorithm based on Fourier fitting for brain function imaging," *Frontiers Physiol.*, vol. 13, Dec. 2022, Art. no. 1054103.

[32] X. Song, X. Chen, J. Guo, M. Xu, and D. Ming, "Living rat SSVEP mapping with acoustoelectric brain imaging," *IEEE Trans. Biomed. Eng.*, vol. 69, no. 1, pp. 75–82, Jan. 2022.

[33] X. Chen, X. Song, J. Guo, G. Han, M. Xu, and D. Ming, "In vivo transcranial measurement of brain-activated sources with acoustoelectric brain imaging," *IEEE Trans. Instrum. Meas.*, vol. 72, pp. 1–10, 2023.

[34] X. Song, X. Su, X. Chen, M. Xu, and D. Ming, "In vivo transcranial acoustoelectric brain imaging of different steady-state visual stimulation paradigms," *IEEE Trans. Neural Syst. Rehabil. Eng.*, vol. 30, pp. 2233–2241, 2022.

[35] X. Song, P. Huang, X. Chen, M. Xu, and D. Ming, "The processing network of high-frequency acoustoelectric signal in the living rat brain," *J. Neural Eng.*, vol. 19, no. 5, Sep. 2022, Art. no. 056013.

[36] A. M. Lozano et al., "Deep brain stimulation: Current challenges and future directions," *Nature Rev. Neurology*, vol. 15, no. 3, pp. 148–160, Jan. 2019.

[37] W. M. Grill, "Temporal pattern of electrical stimulation is a new dimension of therapeutic innovation," *Current Opinion Biomed. Eng.*, vol. 8, no. 1, pp. 1–6, Dec. 2018.

[38] W. M. Grill, "Model-based analysis and design of waveforms for efficient neural stimulation," *Prog. Brain Res.*, vol. 222, pp. 147–162, Dec. 2015.

[39] J. G. V. Jeroen, M. Heijmans, M. L. Kuijf, M. L. F. Janssen, Y. Temel, and P. L. Kubben, "An update on adaptive deep brain stimulation in Parkinson's disease," *Movement Disorders*, vol. 33, no. 12, pp. 1834–1843, Dec. 2018.

[40] F. E. Fox, K. F. Herzfeld, and G. D. Rock, "The effect of ultrasonic waves on the conductivity of salt solutions," *Phys. Rev.*, vol. 70, nos. 5–6, pp. 329–339, Sep. 1946.

[41] J. Jossinet, B. Lavandier, and D. Cathignol, "The phenomenology of acousto-electric interaction signals in aqueous solutions of electrolytes," *Ultrasonics*, vol. 36, nos. 1–5, pp. 607–613, Feb. 1998.

[42] J. Malmivuo and R. Plonsey, *Bioelectromagnetism: Principles and Applications of Bioelectric and Biomagnetic Fields*. New York, NY, USA: Oxford Univ. Press, 1995.

[43] R. Witte, R. Olafsson, S.-W. Huang, and M. O'Donnell, "Imaging current flow in lobster nerve cord using the acoustoelectric effect," *Appl. Phys. Lett.*, vol. 90, no. 16, Apr. 2007, Art. no. 163902.

[44] X.-T. Chen et al., "Effects of Xingnaojing injection on adenosinergic transmission and orexin signaling in lateral hypothalamus of ethanol-induced coma rats," *BioMed Res. Int.*, vol. 2019, no. 1, pp. 1–11, Jun. 2019.

[45] B. Berthon, P.-M. Dansette, M. Tanter, M. Pernot, and J. Provost, "An integrated and highly sensitive ultrafast acoustoelectric imaging system for biomedical applications," *Phys. Med. Biol.*, vol. 62, no. 14, pp. 5808–5822, Jun. 2017.

[46] W. Yi et al., "Enhancing performance of a motor imagery based brain–computer interface by incorporating electrical stimulation-induced SSSEP," *J. Neural Eng.*, vol. 14, no. 2, Apr. 2017, Art. no. 026002.

[47] F. Wan, J. N. da Cruz, W. Nan, C. M. Wong, M. I. Vai, and A. Rosa, "Alpha neurofeedback training improves SSVEP-based BCI performance," *J. Neural Eng.*, vol. 13, no. 3, Jun. 2016, Art. no. 036019.

[48] X. Chen, Y. Wang, M. Nakanishi, X. Gao, T.-P. Jung, and S. Gao, "High-speed spelling with a noninvasive brain–computer interface," *Proc. Nat. Acad. Sci. USA*, vol. 112, no. 44, pp. E6058–E6067, Oct. 2015.

[49] W. M. M. Schüpbach et al., "Directional leads for deep brain stimulation: Opportunities and challenges," *Movement Disorders*, vol. 32, no. 10, pp. 1371–1375, Oct. 2017.

[50] M. Zhang et al., "Decoding coordinated directions of bimanual movements from EEG signals," *IEEE Trans. Neural Syst. Rehabil. Eng.*, vol. 31, pp. 248–259, 2023.

[51] W. Neumann, R. Gilron, S. Little, and G. Tinkhauser, "Adaptive deep brain stimulation: From experimental evidence toward practical implementation," *Movement Disorders*, vol. 38, no. 6, pp. 937–948, Jun. 2023.